ISSN 0036-0295, Russian Metallurgy (Metally), Vol. 2022, No. 10, pp. 1192–1197. © Pleiades Publishing, Ltd., 2022.
Russian Text © The Author(s), 2022, published in Deformatsiya i Razrushenie Materialov, 2022, No. 8, pp. 9–14.

STRUCTURE AND PROPERTIES OF THE DEFORMED STATE

Evolution of the Structure of Rail Steel during Compression

Yu. F. Ivanov[a], V. E. Gromov[b], *, K. V. Aksenova[b], R. V. Kuznetsov[b], V. E. Kormyshev[b], and E. S. Vashchuk[c]

[a] *Institute of High-Current Electronics, Siberian Branch, Russian Academy of Sciences, Tomsk, 634055 Russia*
[b] *Siberian State Industrial University, Novokuznetsk, 654007 Russia*
[c] *Prokop'evsk Branch, Kuzbass State Technical University, Prokop'evsk, 653039 Russia*
**e-mail: gromov@physics.sibsiu.ru*

Received March 30, 2022; revised April 7, 2022; accepted April 12, 2022

Abstract—The evolution of the structure and defect substructure of rail steel during uniaxial compression to a reduction of 50% is studied. The strain hardening is found to have a multistage character and to be accompanied by fragmentation of pearlite grains, which increases with the strain. An increase in the strain is accompanied by a decrease in the scalar and excess dislocation densities. Cementite plates are found to undergo destruction via their dissolution and cutting by mobile dislocations.

Keywords: plastic deformation, uniaxial compression, rail steel, structure, lamellar pearlite, evolution, dislocations

DOI: 10.1134/S0036029522100354

INTRODUCTION

In our country, rail transport is mainly used to perform cargo turnover and passenger traffic. The continuous increase in the requirements for the reliability of rails under conditions of high axle loads and driving speeds necessitates the study of the behavior of rails during long-term operation and an analysis of possible causes for their withdrawal [1]. The investigation of the nature and evolution of structural and phase changes in rail steel during operation is possible by analyzing the deformation behavior of metals under intense plastic deformation [2–4]. Under diverse types and modes of plastic deformation, a fundamental fragmentation phenomenon, i.e., deformation-induced structure refinement to 100–200 nm, is observed in crystalline materials with different types of crystal lattice [5–7].

Pearlitic steel subjected to intense plastic deformation, such as cold drawing at large reductions, can have a ultimate tensile strength of 5 GPa [8]. In [9], tensile tests revealed the following three different types of slip bands in pearlitic steels: bands formed as a result of shear deformation in pearlite colonies, bands at the interface of pearlite colonies, and bands at the ferrite/cementite interface. Using X-ray diffraction analysis during tensile testing of S70 pearlitic steel, the authors of [10] showed that a decrease in the interlamellar spacing by a factor of 1.5 led to an almost twofold increase in the critical shear stress in ferrite. A similar fact was detected in [11], in which a correlation between strain hardening and the evolution of the coherent domain size and the dislocation density was found for pearlitic steel subjected to a microcompression test.

Despite the difference in deformation schemes, the general mechanisms of formation and evolution of the nanostructure of rail steel during plastic deformation are the deformation-induced decomposition of cementite under shear stresses and the subsequent formation of nanoscale tertiary cementite as a result of carbon atom migration [12, 13].

Thus, knowledge of the laws of formation of structural-phase states and properties of steel with a pearlitic structure for various types of plastic deformation is necessary to control the process of strain hardening. The purpose of this work is to analyze the evolution of the structural-phase states of rail steel during plastic deformation by compression.

EXPERIMENTAL

Differentially hardened DT350 rails (Evraz ZSMK) made of degassed E76KhF electric furnace steel in accordance with TU 0921-276-01124333–2021 were studied. The chemical composition of the rail steel is given in Table 1. Rectangular 5 × 5 × 10-mm specimens were cut out of the rail head. Uniaxial compression deformation was carried out at room temperature on an Instron 3369 testing machine at a loading rate of 1.2 mm/min.

The structure of the specimens was examined by transmission electron microscopy (TEM) using a

Table 1. Chemical composition of rail steel, wt %

C	Mn	Si	Cr	P	S	Ni	Cu	Ti	Mo	V	Al
0.73	0.75	0.58	0.42	0.012	0.007	0.07	0.13	0.003	0.006	0.04	0.003

JEOL JEM 2100F microscope [14–16]. Foils were prepared by electrolytic thinning to a thickness of ≈200 nm of plates spark-cut from the middle part of the specimen. The structural-phase state of the steel subjected to deformation by 15, 30, and 50% was analyzed.

The scalar dislocation density of each type of dislocation substructure (DSS) was determined using the methods from [14–17]. It was calculated by the formula

$$\langle\rho\rangle = \frac{M}{t}\left(\frac{n_1}{l_1} + \frac{n_2}{l_2}\right), \quad (1)$$

where n_1 and n_2 are the numbers of intersections of horizontal and vertical lines of length l_1 and l_2, respectively, by dislocations; M is the magnification of a micrograph; and t is the foil thickness (200 nm).

The average scalar dislocation density was determined with allowance for the volume fraction of each type of DSS according to the formula

$$\langle\overline{\rho}\rangle = \sum_{i=1}^{Z} P_{V_i}\rho_i, \quad (2)$$

where P_{V_i} is the volume fraction of the material occupied by the ith type of DSS, Z is the number of types of DSS, and ρ_i is the scalar dislocation density in the ith type of DSS.

The excess dislocation density was calculated using the misorientation gradient [18],

$$\rho_{\pm} = \frac{1}{b}\frac{\partial\varphi}{\partial\lambda}. \quad (3)$$

Here, b is the Burgers vector and $\chi = \frac{\partial\varphi}{\partial\lambda}$ is the lattice curvature–torsion amplitude, where $\partial\varphi$ is the angle of foil inclination in the microscope column and $\partial\lambda$ is the displacement of the extinction contour.

RESULTS AND DISCUSSION

Figure 1a shows the stress–strain curve recorded during uniaxial compression of a specimen. As a rule, the change in the cross-sectional area of a specimen is not taken into account in this method of loading; therefore, this curve should be considered as a conditional compression diagram. For the chosen test method, the specimens could not be brought to fracture: they became flattened. This behavior is explained by the fact that the steel under study is capable of being strongly deformed without fracture in this method of loading.

The stress–strain curve of the steel is a pronounced parabola (see Fig. 1a). An analysis of strain-hardening curves is based on the concept of stages of strain hardening, which reflects the evolution of DSS during deformation [19–21]. In the stress–strain curve (see Fig. 1a), we can distinguish the stage of elastic defor-

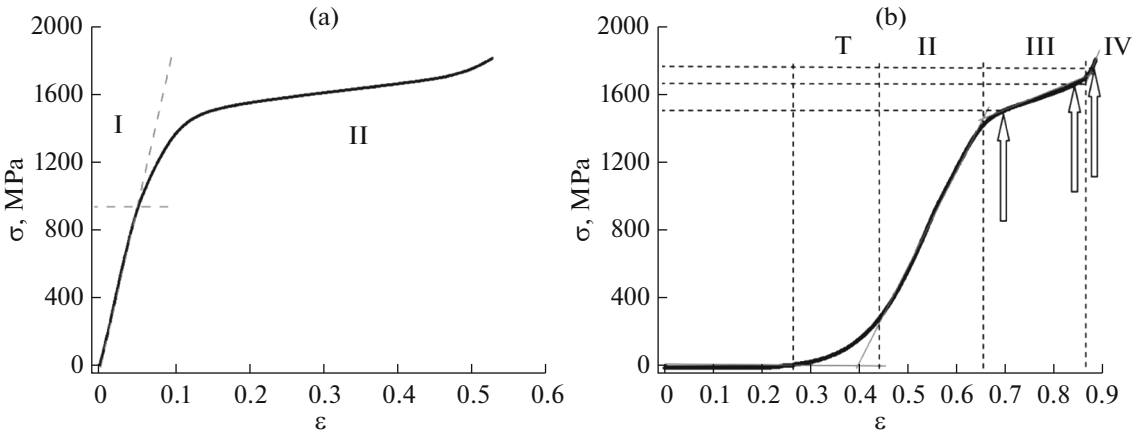

Fig. 1. (a) Stress–strain curve of rail steel during uniaxial compression and (b) its representation in the σ–$\varepsilon^{0.2}$ coordinates. The arrows indicate the parameters of loading the specimens used for a structural-phase investigation.

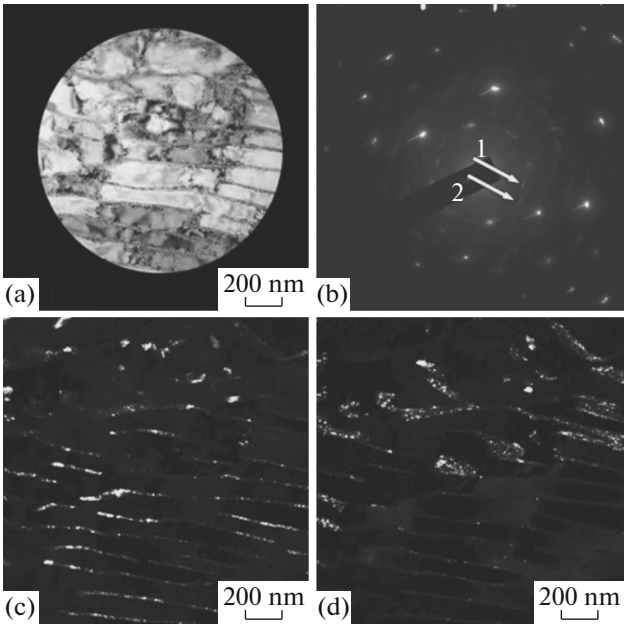

Fig. 2. Structure of the deformed steel (ε = 50%): (a) bright-field image; (b) electron diffraction pattern for (a); and (c, d) dark-field images taken with the [121]Fe_3C and [211]Fe_3C cementite reflections, respectively (indicated by arrows 1 and 2 in (b)).

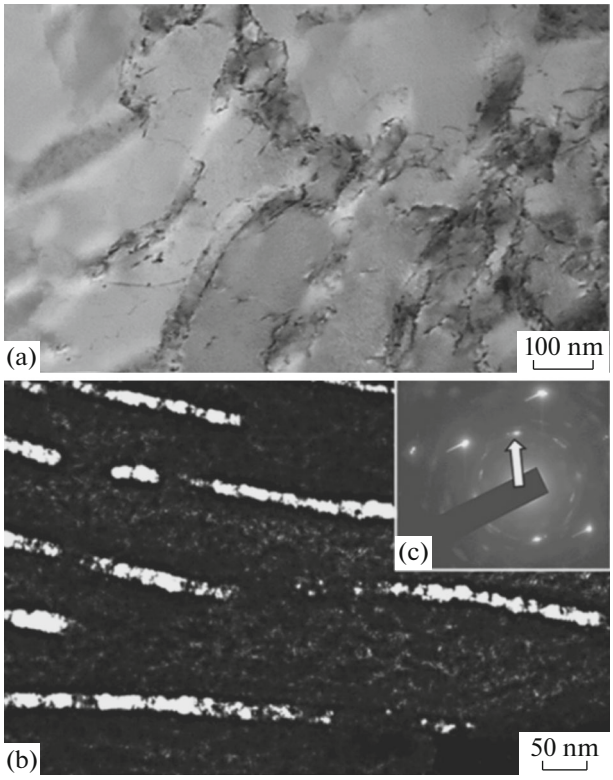

Fig. 3. Structure of the deformed steel (ε = 50%): (a) bright-field image and (b) dark-field image taken with the [012]Fe_3C + [110]α-Fe reflection.

mation (stage I) and the stage of plastic deformation (stage II). In most cases, four stages are distinguished in such a stress–strain curve [19, 20]: transitional (T) stage following the elastic limit and demonstrating either an increase or decrease in the strain-hardening coefficient; stage II with high constant or almost constant high hardening; stage III, at which the strain-hardening coefficient decreases; and stage IV with a very low and a constant strain-hardening coefficient.

Plastic flow stages are associated with a change in a hardening mechanism and, hence, the formation of qualitatively different defect structures. The authors of [21] demonstrated the structural nature of the hardening stages and their relation to linear sections on a stress–strain curve reconstructed in the σ–$\varepsilon^{0.5}$ coordinates. The stages of plastic flow of steel in this work were revealed when stress–strain curves were plotted in the σ–$\varepsilon^{0.2}$ coordinates (Fig. 1b).

The following components were identified in the structure of the initial steel: pearlite of lamellar morphology, ferrite–carbide mixture (degenerate pearlite grains), and structurally free ferrite (ferrite free of carbide phase particles) at their relative contents of 0.7, 0.26, and 0.04, respectively. DSS in the form of chaotically distributed dislocations or, less frequently, dislocation networks is observed in the volume of all structural constituents. The scalar dislocation density determined by the techniques from [14–17] is $\langle\rho\rangle = 3.2 \times 10^{10}$ cm^{-2} in ferrite grains and $\langle\rho\rangle = 4.2 \times 10^{10}$ cm^{-2} in pearlite grains.

The multiple transformation of a pearlite structure consists primarily in fragmentation, which increases with the degree of deformation. At ε = 50%, the volume of a fragmented structure is 0.37 of the foil volume. When the degree of deformation increases, the average ferrite plate fragment size decrease from 240 nm at ε = 15% to 200 nm at ε = 50%.

Simultaneously with ferrite plates, fragmentation of cementite plates was also revealed (Fig. 2): their sizes are 15–20 nm and weakly depend on the degree of deformation. Along with fragmentation, the destruction of cementite plates was also noted. The first mechanism of destruction consists in cutting plates by moving dislocations and picking up carbon atoms by dislocations to their stress field [22]. The second mechanism consists in pulling carbon atoms out of the cementite lattice during plastic deformation by dislocations due to a noticeable difference in the average energies of binding carbon atoms with dislocations (0.6 eV) and iron atoms in (0.4 eV) the cementite lattice. Carbon atoms transferred from the cementite lattice to dislocations are moved to the interlamellar spacing and form tertiary cementite particles (Fig. 3). The sizes of such particles are 2–4 nm.

The deformation of pearlite grains is accompanied by the transformation of the DSS of steel. For example, dislocations are distributed quasi-uniformly over

the volume of ferrite plates in the structure of the initial steel, and dislocation pileups form around cementite particles during deformation.

An increase in the degree of deformation was found to be accompanied by a decrease in the scalar density of dislocations located in the volume of fragments (Table 2). This decrease can be caused by the departure of dislocations into low-angle boundaries and their annihilation. A similar change in the DSS of fragments formed during deformation was observed in [23].

We now determine the density of dislocations forming low-angle fragment boundaries. As was shown in [14–17, 24] the dislocation density in low-angle boundaries can be estimated at a given misorientation angle between fragments Θ, Burgers vector b of dislocations in a low-angle boundary, and average fragment size d,

$$\langle\rho_b\rangle = \frac{2\Theta}{bd}. \quad (4)$$

The angle of misorientation between fragments (Fig. 4a) was determined using a certain electron diffraction pattern and the relation [24]

$$\Theta = \frac{\Delta}{R}, \text{ rad},$$

where Δ is the diffraction maximum width and R is the radius vector of this reflection (Fig. 4b).

Assuming $b = 0.25$ nm and average fragment size $d = 200$ nm, we use Eq. (4) and obtain $\rho_b = 0.002$ nm^{-2} = 2.0×10^{11} cm^{-2}. Taking into account that the relative content of pearlite with a fragmented structure at ε = 50% is ≈0.37, we finally obtain the density of the dislocations concentrated in low-angle fragment boundaries of the steel under study, $\rho_b = 0.37 \times 2.0 \times 10^{11}$ cm^{-2} = 7.4×10^{10} cm^{-2}. At a certain degree of conditionality, this is thought to be the dislocation density in steel at ε = 50%, and this is no longer a scalar dislocation density.

The deformation of steel is not only accompanied by pearlite fragmentation, but also leads to the formation of dislocation pileups around cementite particles.

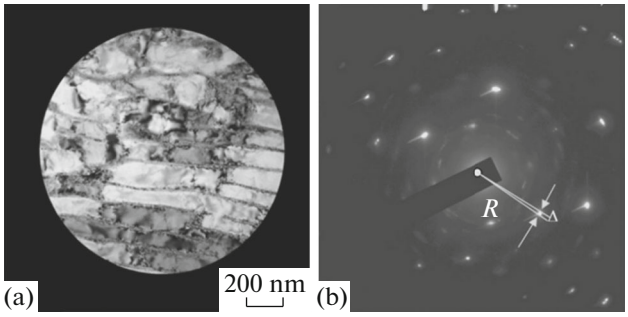

Fig. 4. (a) Structure of the steel deformed at ε = 50% and (b) electron diffraction pattern taken from the given foil area; the arrows indicate the reflection used to determine the angle of complete misorientation of the steel structure.

Table 2. Scalar $\langle\rho\rangle$ and excess $\rho_\pm$ dislocation densities in fragments as functions of strain ε

Parameter	Dislocation density, 10^{10} cm^{-2}, at ε, %			
	0	15	30	50
$\langle\rho\rangle$	2.5	2.1	1.6	0.6
$\rho_\pm$	1.8	1.6	1.0	0.3

The dislocation density at cementite particles is estimated by Eq. (1). For the steel structure shown in Fig. 5, we have $M = 44 \times 10^4$, $t = 200 \times 10^{-7}$ cm and obtain $\langle\rho\rangle = 9.8 \times 10^{10}$ cm^{-2}. Taking into account that the content of pearlite with a fragmented structure is 0.37, we assume that the rest of the steel structure (0.63) is occupied by particles surrounded by dislocations, as is shown in Fig. 5. In this case, the scalar dislocation density in the steel at ε = 50% is $\langle\rho\rangle = 0.63 \times 9.8 \times 10^{10}$ cm^{-2} = 6.2×10^{10} cm^{-2}.

TEM analysis of the DSS of the deformed steel revealed bending extinction contours on electron microscopic images of the structure. Their presence indicates bending–torsion of the crystal lattice in this region of the material and, consequently, internal fields stresses, which bend a thin foil and, accordingly, strengthen the material [1, 25, 26].

One of the characteristics of the curvature–torsion of the crystal lattice is excess dislocation density $\rho_\pm$. The estimation showed that $\rho_\pm$ decreases like the scalar density of dislocations with an increase in the strain (see Table 2). The lower values of $\rho_\pm$ as compared to $\langle\rho\rangle$ can be associated with the broadening of extinction

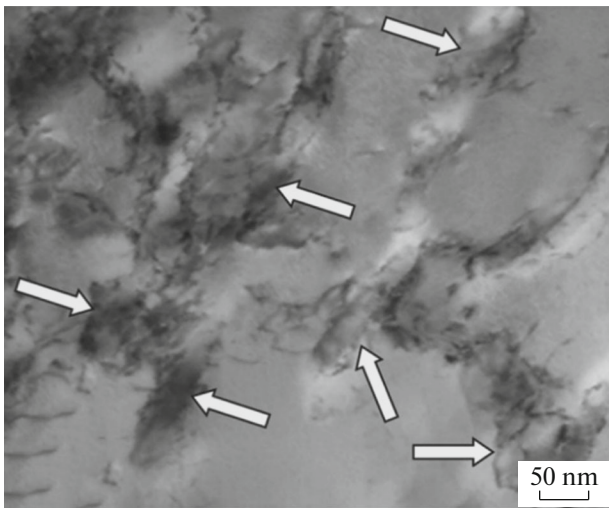

Fig. 5. DSS of the steel deformed at ε = 50% near cementite particles (indicated by arrows).

contours during deformation, which leads to a decrease in the fragment size.

CONCLUSIONS

(1) The deformation of rail steel is accompanied by the fragmentation of pearlite grains, which increases with the degree of deformation and reaches ≈0.4 of the material volume at $\varepsilon = 50\%$. The fragment sizes of ferrite plates are 240 and 200 nm at $\varepsilon = 15$ and 50%, respectively, and the fragmentation of cementite plates weakly depends on the degree of deformation.

(2) The destruction of cementite plates proceeds via their dissolution and cutting by mobile dislocations. The carbon atoms having passed from the crystal lattice of cementite to dislocations are moved into the interlamellar space and form tertiary cementite particles, the size of which is 2–4 nm.

(3) The formation of an inhomogeneous DSS during the deformation of steel is caused by the retardation of dislocations by cementite particles.

(4) An increase in the degree of deformation is accompanied by a decrease in the scalar and excess dislocation densities, which can be due to the departure of dislocations into low-angle boundaries and their annihilation.

ACKNOWLEDGMENTS

We thank E.V. Polevoi for providing the rail steel specimens and N.A. Popova for helpful discussions.

FUNDING

This work was supported by the Russian Foundation for Basic Research (project no. 19-32-60001) and a scholarship of the President of the Russian Federation for young scientists and postgraduates engaged in promising research and development in priority areas of modernization of the Russian economy (project no. SP-4517.2021.1).

CONFLICT OF INTEREST

The authors declare that they have no conflicts of interest.

REFERENCES

1. A. A. Yuriev, Yu. F. Ivanov, V. E. Gromov, Yu. A. Rubannikova, M. D. Starostenkov, and P. Y. Tabakov, *Structure and Properties of Lengthy Rails after Extreme Long-Term Operation* (Materials Research Forum LLC, Millersville, 2021).
2. Y. Wang, Y. Tomota, S. Harjo, W. Gong, and T. Ohmuraa, "In- situ neutron diffraction during tension-compression cyclic deformation of a pearlite steel," Mater. Sci. Eng., A **676**, 522–530 (2016).
3. R. Pan, R. Ren, C. Chen, and X. Zhao, "Formation of nanocrystalline structure in pearlitic steels by dry sliding wear," Mater. Charact. **132**, 397–404 (2017).
4. M. W. Kapp, A. Hohenwarter, S. Wurster, B. Yang, and R. Pippan, "Anisotropic deformation characteristics of an ultrafine- and nanolamellar pearlitic steel," Acta Mater. **106**, 239–248 (2016).
5. D. Raabe and R. Kumar, "Tensile deformation characteristics of bulk ultrafine-grained austenitic stainless steel produced by thermal cycling," Scr. Materialia. **66**, 634–637 (2012).
6. M. K. Skakov, G. K. Uazyrkhanova, N. A. Popova, and M. Scheffler, "Influence of heat treatment and deformation on the phase-structural state of steel 30CrMnSiA," Key Eng. Mater. **531–532**, 13–17 (2013).
7. J. Zrnik, S. Dobatkin, G. Raab, M. Fujda, and L. Kraus, "Ultrafine grain structure development in steel with different initial structure by severe plastic deformation," Revista Materia **15** (2), 240–246 (2010).
8. T. Takahashi, I. Ochiai, H. Tashiro, S. Ohashi, S. Nishida, and T. Tarui, "Strengthening of steel wire for tire cord," Nippon Steel Tech. Report **64**, 45–49 (1995).
9. Y. Zhao, Y. Tan, X. Ji, Z. Xiang, and S. Xiang, "In situ study of cementite deformation and its fracture mechanism in pearlitic steels," Mater. Sci. Eng., A **731**, 93–101 (2018).
10. H. Yahyaoui, H. Sidhom, C. Braham, and A. Baczmanski, "Effect of interlamellar spacing on the elastoplastic behavior of C70 pearlitic steel: experimental results and self-consistent modeling," Mater. Design **55**, 888–897 (2014).
11. M. Ekh, N. Larijani, E. Dartfeldt, M. Kapp, and R. Pippan, "Prediction of the mechanical behaviour of pearlitic steel based on microcompression tests, micromechanical models and homogenization approaches," Eur. J. Mech.: A. Solids **67**, 272–279 (2018).
12. Y. J. Li, P. Choi, C. Borchers, S. Westerkamp, S. Goto, D. Raabe, and R. Kirchheim, "Atomic-scale mechanisms of deformation-induced cementite decomposition in pearlite," Acta Mater. **59**, 3965–3977 (2011).
13. H. Yahyaoui, H. Sidhom, C. Braham, and A. Baczmanski, "Effect of interlamellar spacing on the elastoplastic behavior of C70 pearlitic steel: experimental results and self-consistent modeling," Mater. Design **55**, 888–897 (2014).
14. F. R. Egerton, *Physical Principles of Electron Microscopy* (Springer, Basel, 2016).
15. C. S. S. R. Kumar, *Transmission Electron Microscopy. Characterization of Nanomaterials* (Springer, New York, 2014).
16. C. B. Carter and D. B. Williams, *Transmission Electron Microscopy* (Springer, Berlin, 2016).
17. P. Hirsch, A. Howie, R. Nicholson, D. Pashley, and M. Whelan, *Electron Microscopy of Thin Crystals* (Plenum, New York, 1967).
18. N. A. Koneva, D. V. Lychagin, L. A. Teplyakova, and E. V. Kozlov, "Crystal lattice rotation and the stages of plastic deformation," in *Experimental Study and Theoretical Description of Disclinations* (FTI, Leningrad, 1984), pp. 161–164.

19. U. F. Kocks and H. Mesking, "Physics and phenomenology of strain hardening: the FCC case," Prog. Mater. Sci. **48**, 171–279 (2003).

20. Yu. N. Podrezov and S. A. Firstov, "Two approaches to an analysis of stress–strain curves," Fiz. Tekh. Vys. Davl. **16** (4), 37–48 (2006).

21. V. I. Trefilov, V. F. Moiseev, E. P. Pechkovskii, and I. D. Gornaya, *Strain Hardening and Fracture of Polycrystalline Materials* (Naukova Dumka, Kiev, 1989).

22. V. N. Gridnev and V. G. Gavrilyuk, "Decomposition of cementite during plastic deformation," Metallofiz. **4** (3), 74–87 (1982).

23. E. V. Kozlov, N. A. Popova, and N. A. Koneva, "Scalar dislocation density in fragments with different types of substructure," Pis'ma Mater. **1**, 15–18 (2011).

24. L. M. Utevskii, *Diffraction Electron Microscopy in Physical Metallurgy* (Metallurgiya, Moscow, 1973).

25. Yu. F. Ivanov, V. E. Gromov, and E. N. Nikitina, *Bainite Constructional Steel: Structure and Properties* (CISP, Cambridge, 2016).

26. Yu. F. Ivanov, E. V. Kornet, E. V. Kozlov, and V. E. Gromov, *Hardened Structural Steel: Structure and Hardening Mechanisms* (Izd. SibGIU, Novokuznetsk, 2010).

Translated by K. Shakhlevich